Supplementary Information

Room temperature multiferroicity in a transition metal dichalcogenide

G. Cardenas-Chirivi[1,2], K. Vega-Bustos[1], H. Rojas-Páez[1], D. Silvera-Vega[1], J. Pazos[2], O. Herrera[2], M. A. Macías[3], C. Espejo[4], W. López-Pérez[4], J. A. Galvis[5] and P. Giraldo-Gallo[1,*]

[1] Department of Physics, Universidad de Los Andes, Bogotá 111711, Colombia
[2] Faculty of Engineering and Basic Sciences, Universidad Central, Bogotá, Colombia
[3] Department of Chemistry, Universidad de Los Andes, Bogotá 111711, Colombia
[4] Department of Physics and Geosciences, Universidad del Norte, Barranquilla, Colombia
[5] School of Engineering, Science and Technology, Universidad del Rosario, Bogotá 111711, Colombia
[*] Corresponding author: pl.giraldo@uniandes.edu.co

(Dated: August 10th, 2023)

Supplementary Note 1: Chemical composition of single crystals

Chemical compositions for all single crystals were determined through XRF measurements, by triplication. According to the stoichiometric formula, $W(Se_{1-x}Te_x)_{2(1-\delta)}$, percentages of tellurium doping and chalcogen vacancies are presented in Supplementary Table 1. The "Nominal Composition" column presents the aimed Te-doping and chalcogen vacancies concentration, used to calculate the stoichiometric fractions of elemental precursors during the initial sintering process. However, the real compositions, determined through XRF, differ considerably from the nominal values, as shown in the last two columns (real concentrations of Te and vacancies).

Several Te-doping concentrations were obtained. In addition, two undoped compositions with a high-level of vacancies (x=0%, δ=50%) were synthesized in order to discriminate the effects of Te-doping and chalcogen vacancies in the observed properties.

Nominal composition		**Element**			**Real tellurium doping, x (%)**	**Real chalcogen vacancies, δ (%)**
		W	**Se**	**Te**		
x=0% δ=0%	Mass (%)	55 ± 2	45 ± 2	-	0	4 ± 6
	moles	1.00 ± 0.03	1.9 ± 0.1	-		
x=0% δ=50%	Mass (%)	56.1 ± 0.1	43.9 ± 0.1	-	0	8.7 ± 0.2
	moles	1.000 ± 0.001	1.824 ± 0.005	-		
x=0% δ=50%	Mass (%)	56.99 ± 0.84	43.01 ± 0.84	-	0	12 ± 3
	moles	1.00 ± 0.01	1.75 ± 0.04	-		
x=2% δ=0%	Mass (%)	53.82 ± 0.08	45.3 ± 0.5	0.7 ± 0.4	1.0 ± 0.5	1 ± 2
	moles	1.000 ± 0.001	1.96 ± 0.02	0.02 ± 0.01		

***x*=5%** ***δ*=0%**	Mass (%)	56 ± 1	43 ± 1	1.08 ± 0.06	1.45 ± 0.08	9 ± 3
	moles	1.00 ± 0.02	1.78 ± 0.06	0.028 ± 0.002		
***x*=50%,** ***δ*=0%**	Mass (%)	64 ± 3	31 ± 3	5.4 ± 0.3	7.6 ± 0.6	38 ± 6
	moles	1.00 ± 0.04	1.1 ± 0.1	0.12 ± 0.01		
***x*=50%,** ***δ*=0%**	Mass (%)	57 ± 3	32 ± 4	11 ± 1	15 ± 2	21 ± 11
	moles	1.00 ± 0.04	1.3 ± 0.2	0.27 ± 0.04		

Supplementary Table 1. Chemical composition of single crystals, determined through X-ray Fluorescence Spectroscopy (XRF).

Supplementary Note 2: Raman and XRD spectra

In Supplementary Figure 1, Raman spectra are shown for all Te-doped compositions and an undoped one, for a wide range of Raman shifts. A decrease in the Raman shift of the E_{2g} and A_{1g} modes of the 2H-structure, with increasing Te-concentration is observed.

On the other hand, X-ray powder diffraction (XRD) patterns of $W(Se_{1-x}Te_x)_{2(1-\delta)}$ single crystals for all doped compositions and an undoped one are presented in Supplementary Figure 2. Here, reported XRD peak positions for pure 2H-WSe_2 [33] are added for comparison. A continuous shift to lower angle is observed in the {001} family peak positions with increasing Te-doping. This allows us to conclude that inclusion of tellurium in the 2H-phase enhances the c-lattice parameter with respect to the undoped one.

Supplementary Table 2 presents the obtained lattice constants, obtained through powder x-ray diffraction and single crystal diffraction, as explained in the methods section. For the powder x-ray diffraction, the values shown in the table are the average over different peaks of the same family.

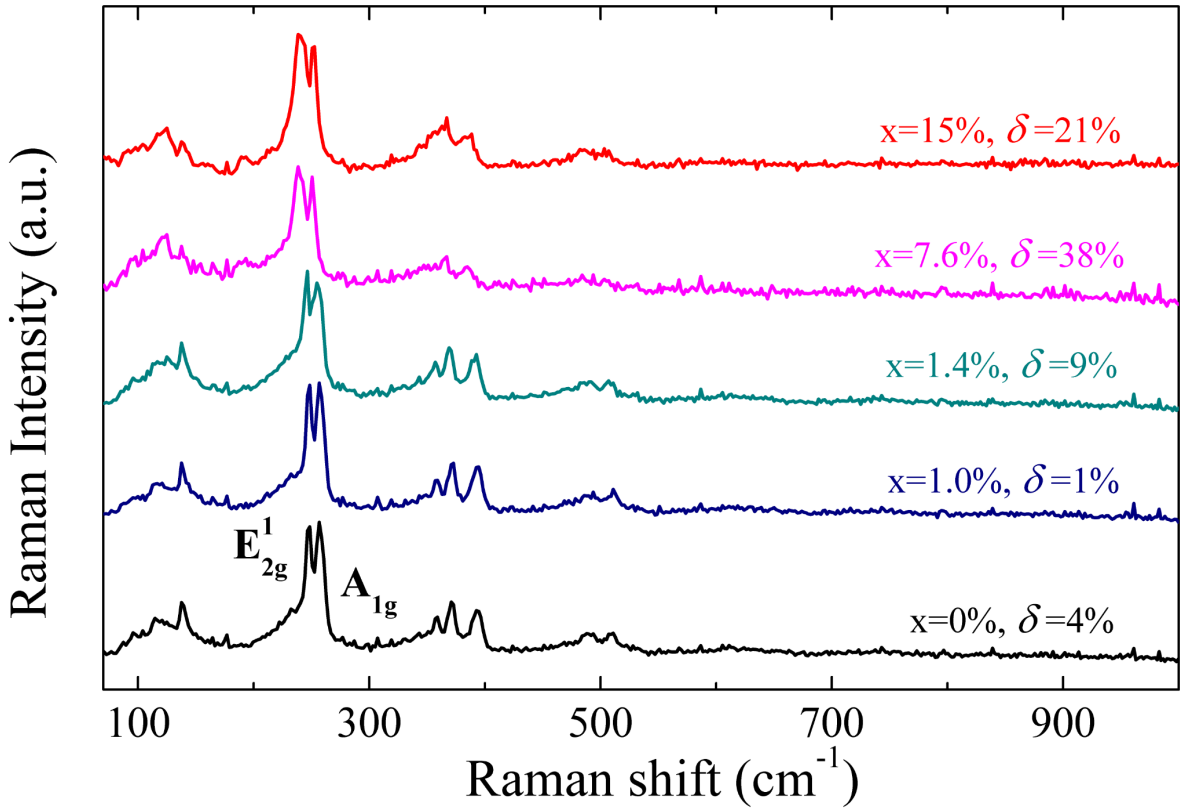

Supplementary Figure 1. Raman spectroscopy measurements. Raman spectra for all tellurium-doped single crystals involved in this study.

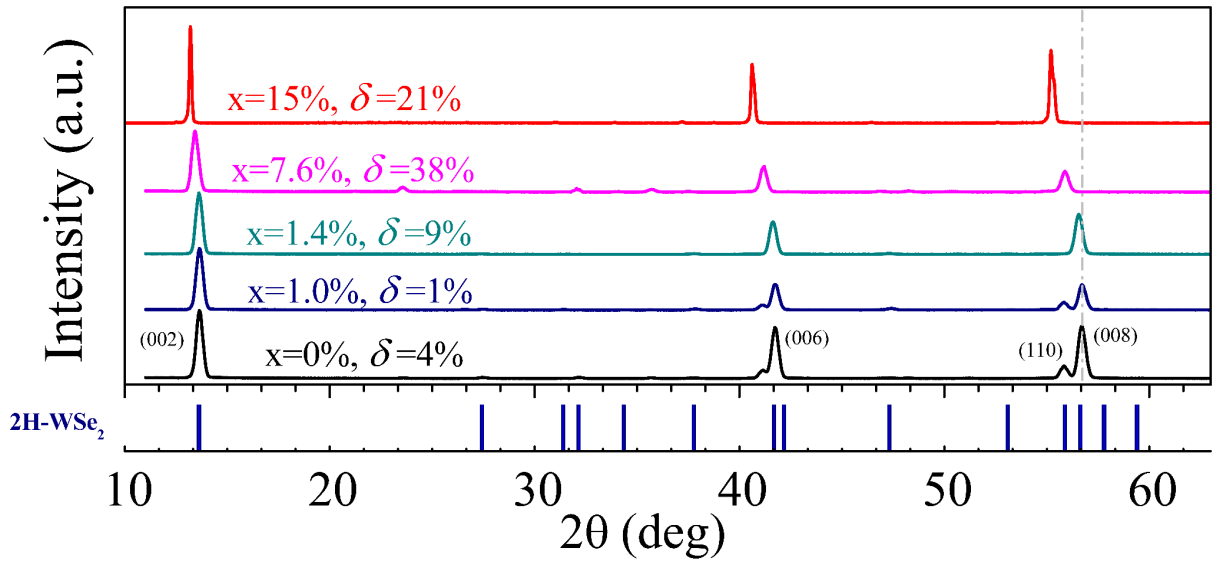

Supplementary Figure 2. X-ray diffraction measurements. XRD patterns for all tellurium-doped single crystals involved in this study. Vertical blue lines show the expected diffraction peaks for the 2H-structure of WSe_2.

Tellurium doping (x, %)	Powder X-ray Diffraction		Single crystal X-ray Diffraction	
	a (Å)	c (Å)	a (Å)	c (Å)
0	3.287 ± 0.008	12.974 ± 0.009	-	-
1.0	3.28 ± 0.01	12.99 ± 0.03	3.2857± 0.0005	12.9773 ± 0.0015
1.4	3.288 ± 0.003	13.004 ± 0.008	-	-
7.6	3.28 ± 0.01	13.16 ± 0.02	3.3074± 0.0005	13.180 ± 0.002
15	3.34 ± 0.01	13.3 ± 0.1	-	-

Supplementary Table 2. X-ray diffraction results. Lattice constants for all compositions, found by X-ray diffraction measurements.

Supplementary Note 3: Magnetic properties

Supplementary Figure 3(a) shows the total magnetization in emu/g at 300K for x=0-15% tellurium-doped compositions. Here, the magnetic response reveals two components: a diamagnetic and a ferromagnetic contribution. The ferromagnetic component, obtained by subtracting the linear-diamagnetic contribution of each curve, has a slight temperature dependence, particularly in the saturation magnetization, as evidenced in Supplementary Figure 3(b) which shows measurements at 80 K and 300 K for different Te-compositions.

On the other hand, the diamagnetic component has a strong dependence with the level of oxidation of the samples. Supplementary Figures 4(a,b) show the total magnetization curves for two types of samples, comparing the results for two different levels of exposure to ambient conditions: short after synthesis (short exposure-time to ambient conditions), and after several days of storage in low vacuum (see methods for storage conditions). For the curves it is clear that the diamagnetic slope is developed only after a prolonged exposure to ambient conditions, whereas the ferromagnetic contribution of the magnetization is present with and without exposure to oxygen. Moreover, the ferromagnetic contribution seems to be more robust to slight oxidation of the samples, as shown in Supplementary Figures 4(c,d). These curves reveal that the coercive field of the ferromagnetic hysteresis loops present only slight variations with the level of exposure to ambient conditions. Supplementary Table 3 shows the variation in coercive field and saturation magnetization of the ferromagnetic contribution to magnetization, for different times of exposure to oxygen, for four different types of samples. Although the saturation magnetization presents variations with the time of exposure to oxygen, the coercive field is very robust to the oxidation level, and this is the reason why this quantity was the one chosen to study the evolution of the magnetism with Te-doping and chalcogen vacancy level.

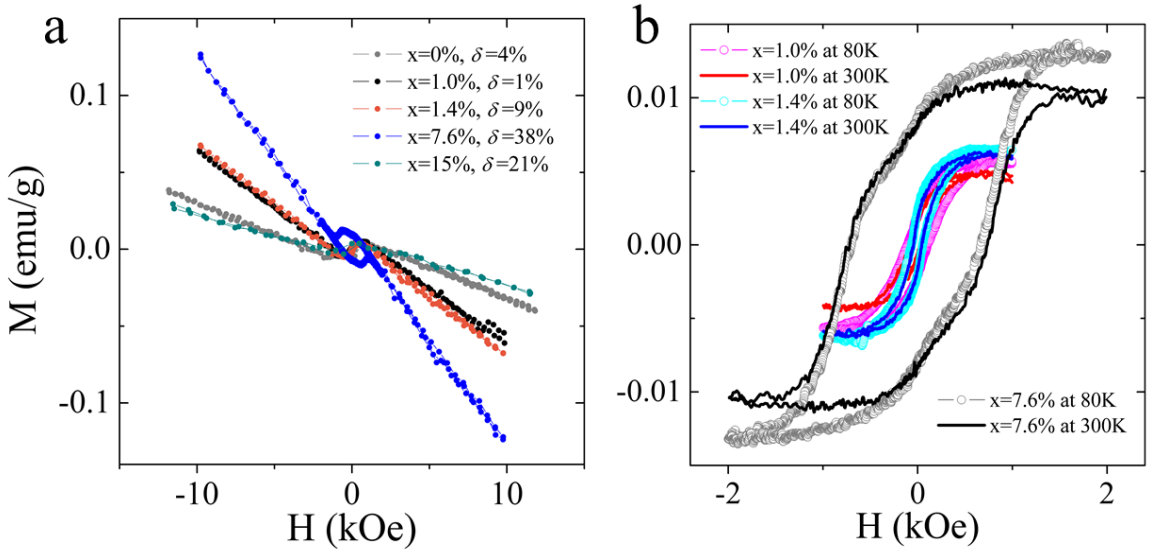

Supplementary Figure 3. Magnetization measurements. (a) Total magnetization measurements at 300 K for all tellurium-doped samples **(b)** Ferromagnetic contribution in the magnetization for tellurium-doped (x=1.0-7.6%) single crystals at 300K and 80K.

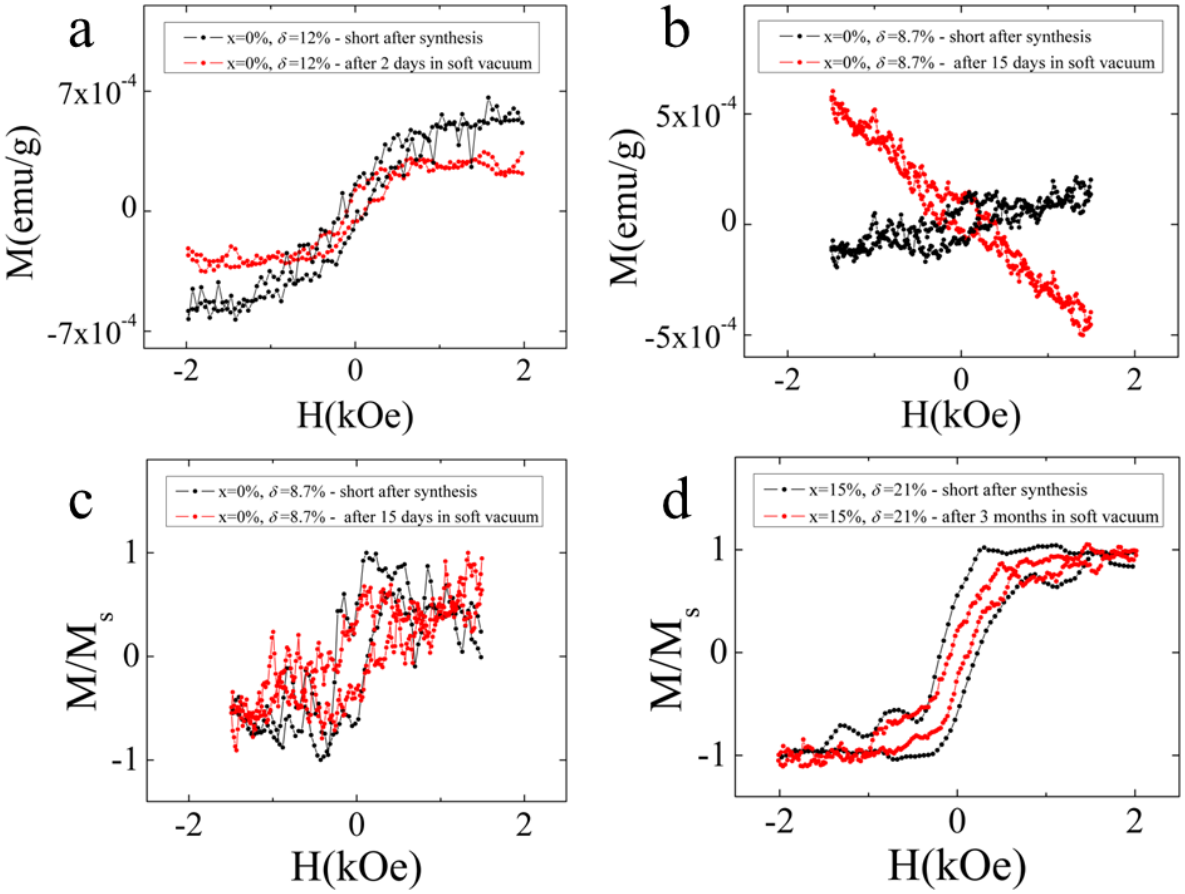

Supplementary Figure 4. Exposure time dependance of magnetization measurements. (a,b) Total magnetization hysteresis loops, for two different times of exposure to ambient conditions, for samples without Te-doping and vacancy level of **(a)** δ=12%, and **(b)** δ=8.7%. **(c,d)** Ferromagnetic contribution to the magnetization for two different times of exposure to ambient conditions, for **(c)** the undoped sample with δ=8.7% and **(d)** the Te doped sample with x=15%, δ=21%.

Magnetic property		XFR Compositions			
		***x*=0% *δ*=12%**	***x*=1% *δ*=1%**	***x*=0% *δ*=8.7%**	***x*=15% *δ*=21%**
	Storage time (days)	2	3	15	90
H_c	Short after synthesis (Oe)	113 ± 25	47 ± 34	199 ± 20	188 ± 25
	After low vacuum storage (Oe)	113 ± 10	47 ± 15	169 ± 40	91 ± 18
	(%) var	0.00 ± 0.04	0.0 ± 0.5	-15 ± 4	-52 ± 10
M_s	Short after synthesis (memu/g)	0.53 ± 0.06	8 ± 1	0.13 ± 0.05	2.7 ± 0.6
	After low vacuum storage (memu/g)	0.28 ± 0.07	4.8 ± 0.4	0.12 ± 0.06	0.52 ± 0.07
	(%) var	- 47 ± 12	- 40 ± 3	- 8 ± 3	- 81 ± 11

Supplementary Table 3. Variation in ferromagnetic properties after low vacuum storage.

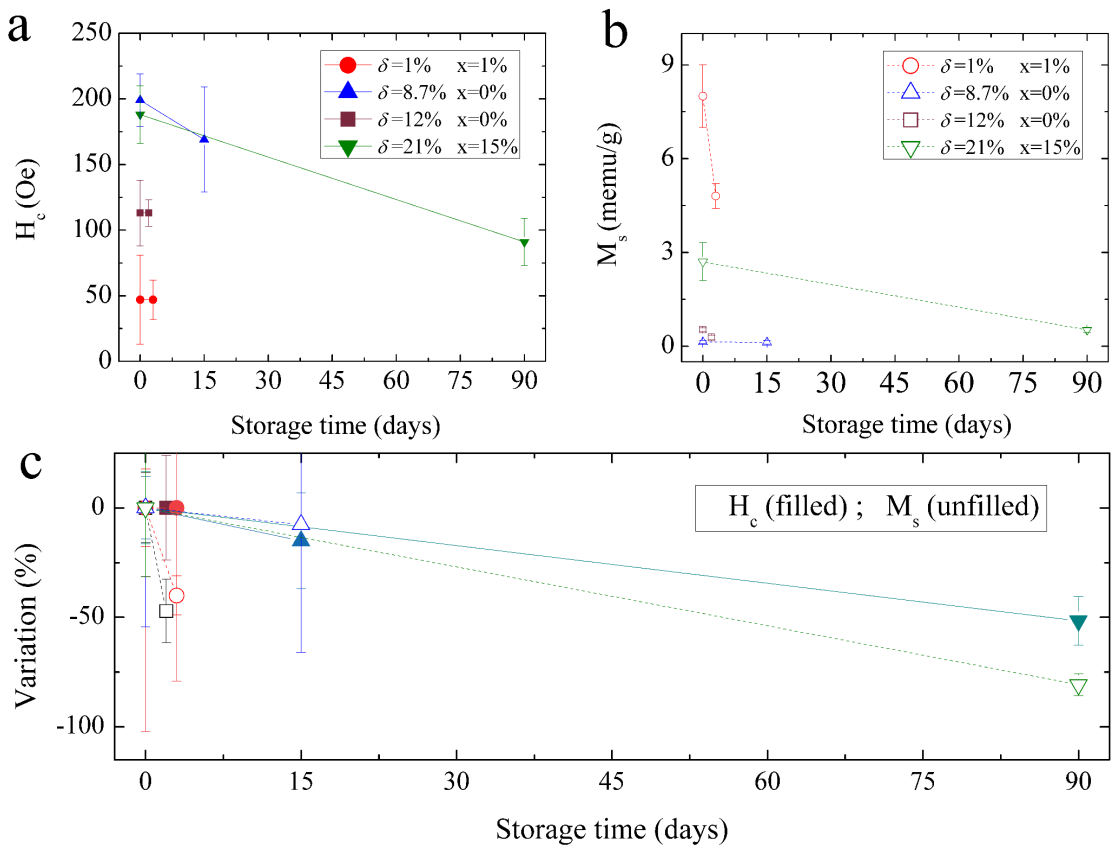

Supplementary Figure 5. Storage time dependance of ferromagnetic properties. (a) Coercive field (H_c) and **(b)** saturation magnetization (M_s) as a function of storage time in low vacuum conditions. Error bars for H_c were obtained by error propagation of the maximum dispersion around the *M=0* axis of the plus and minus field H_c. Error bars for M_s were calculated by the maximum data dispersion around the average M_s value for positive fields. **(c)** Comparative plot of the percentage of variation of both, H_c and *M*s, as a function of storage time. Although both H_c and M_s vary with time, the percentage variation is more pronounced for M_s than for H_c for most samples. Error bars were calculated by error propagation of the H_c and *M*s errors.

Supplementary Note 4: PFM measurements in periodically poled lithium niobate (PPLN)

In order to check the calibration of our PFM experimental setup, and to gain confidence on the accuracy of the reported values for the piezoelectric coefficients of our single crystals, we performed DART-PFM and SS-PFM measurements in a commercially available Periodically Poled Lithium Niobate (PPLN) sample. Supplementary Figure 6(a) shows the results of the DART-PFM measurements, in which the deformation amplitude is scanned in an area of about 3 um x 3 um, and for different applied AC bias voltages, ranging from 0.5 V to 1.25 V. The amplitude values were normalized by the SHO model. The spatial average of deformation amplitude is plotted as a function of bias voltage in Supplementary Figure 6(b). The slope of the linear regression to this curve corresponds to the piezoelectric coefficient, d_{33}. For our sample of PPLN, the experimental result d_{33} is 19.00 ± 1.18 pm/V. This value is similar to the reported values for d_{33} in multiple piezoelectric studies for PPLN [31]. Therefore, this demonstrates that the presented method is reliable for the determination of effective piezoelectric constants.

Supplementary Figure 7 shows additional PFM measurements on the same PPLN sample. DART-PFM measurements (Supplementary Figures 7(a-c)) allow the identification of poled domains in this material, which are not visible on the topography image. These domains were investigated by SS-PFM over the marked points in Supplementary Figure 7(c). Firstly, both, $+z$ poled and $-z$ poled regions were measured using DC pulses bias from 0 to ±1 V. The SS-PFM phase shows that these domains are oriented in opposite directions. Their SS-PFM amplitudes reveal an opposite behavior on the sample deformation: a contraction for $-z$ poled and an extension for $+z$ poled (Supplementary Figure 7(d)).

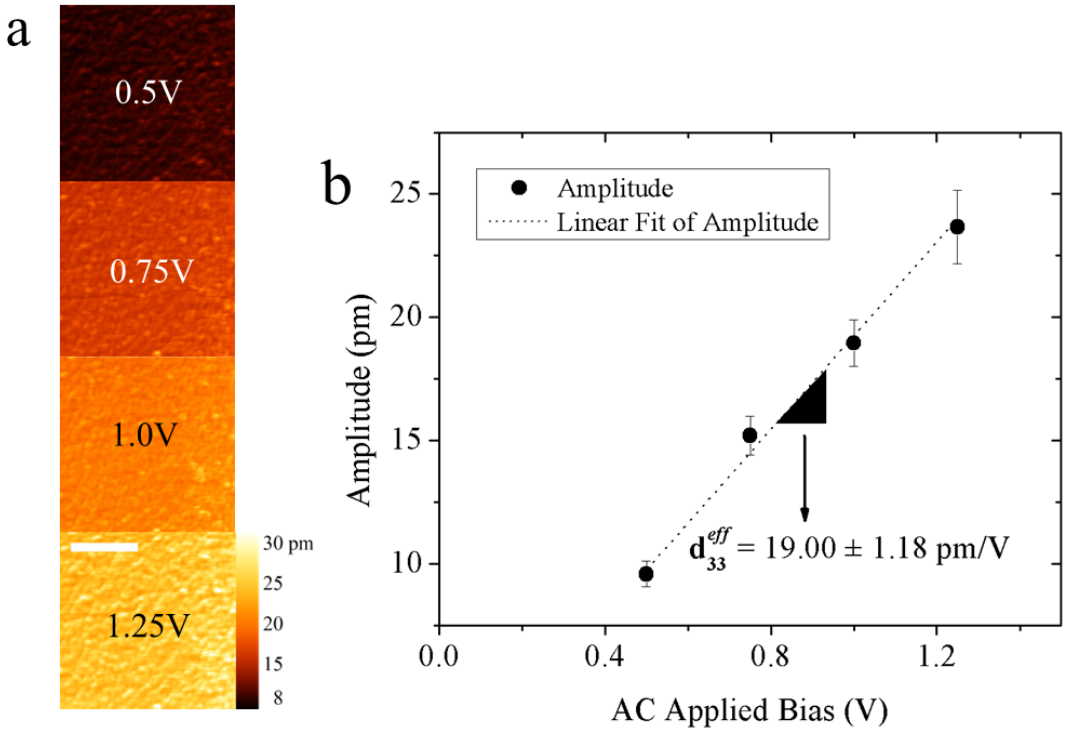

Supplementary Figure 6. DART-PFM measurements of a periodically poled lithium niobate (PPLN) sample. **(a)** DART-PFM piezoresponse normalized by SHO model as a function of the AC applied bias for PPLN material, and **(b)** their resultant effective d_{33}. Scale bar: 1 µm. Error bar for each point represents the standard deviation of the amplitude within each image for each voltage.

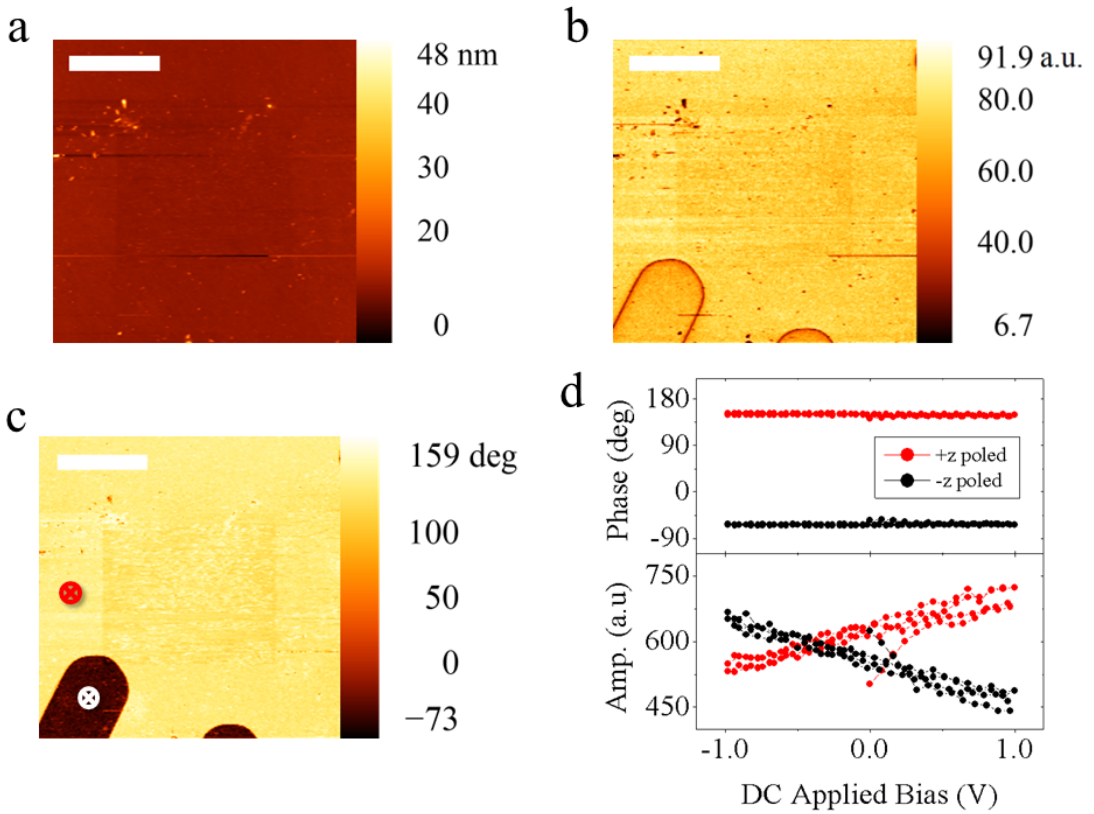

Supplementary Figure 7. Other PFM measurements of a PPLN sample. (a) Topography and DART-PFM **(b)** amplitude and **(c)** phase. Scale bar: 5 μm. **(d)** SS-PFM amplitude and phase for a DC pulses bias from 0 to ±1 V in ±*z*-poled points shown in (c).

Supplementary Note 5: Piezoresponse force microscopy hysteresis loops

Switching Spectroscopy (SS) PFM hysteresis loops for all tellurium-doped compositions, and an undoped sample (x=0%, δ=4%), are compared in Supplementary Figure 8. Given that the undoped sample - which is not piezoelectric - was measured in the same conditions as the Te-doped samples, it can be used to identify the contribution of electrostatic effects during the measurement. It is worth noting that those contributions are negligible when compared to the experimental signal in our Te-doped compositions. Significantly, the amplitude of the SS-PFM signal increases enormously with increasing tellurium doping, which confirms the large enhancement of the piezoelectric coefficient for the highest Te-doping sample.

The ferroelectric states, just as ferromagnetic states, are affected by possible sample oxidation due to long-time storage in a low vacuum desiccator. Interestingly, both the ferromagnetic (see Supplementary Figure 4d for sample with x=15%, δ=21%) and ferroelectric (see Supplementary Figure 9 for a sample with the same composition) signals are not fully suppressed after 4 months of storage, although they get noticeably weakened. After 10 months since synthesis, the ferroelectric hysteresis cannot longer be distinguished, although a considerable piezoelectric effect is still present.

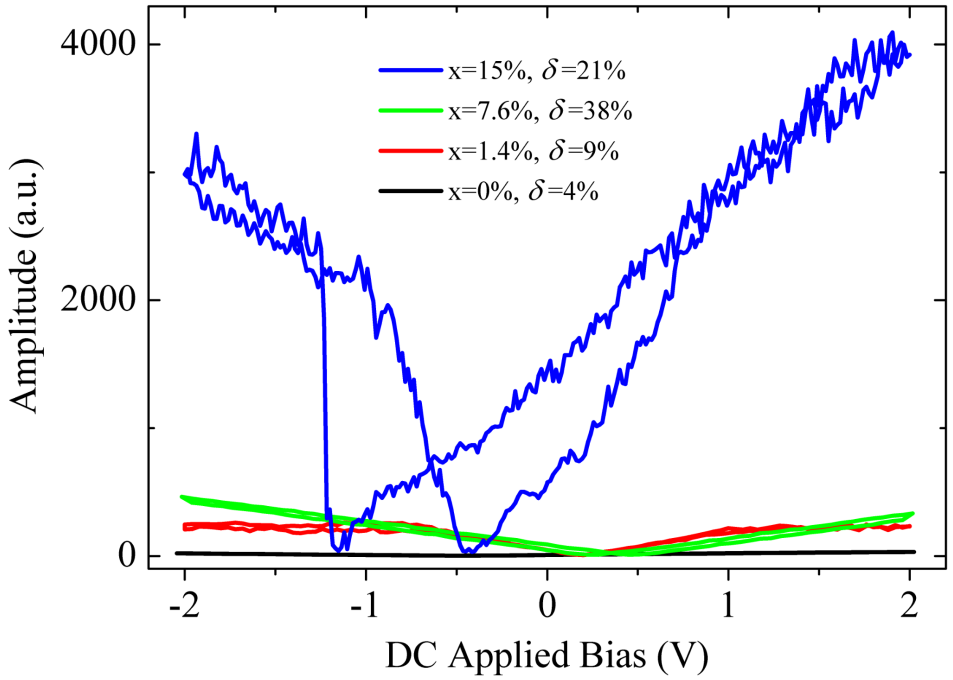

Supplementary Figure 8. Switching Spectroscopy (SS) PFM hysteresis loops, at 300 K under an inert atmosphere for all tellurium-doped compositions. An undoped composition (black) is measured to illustrate contributions to the amplitude caused by electrostatic effects.

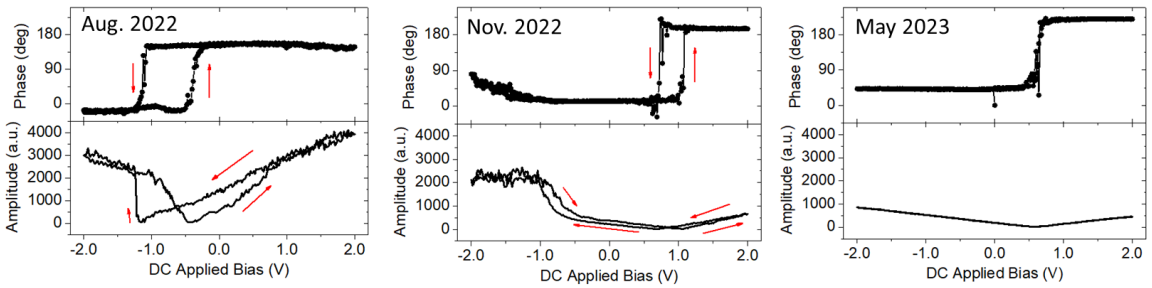

Supplementary Figure 9. Storage time dependance of ferroelectric properties. Switching Spectroscopy (SS) PFM hysteresis loops (phase and amplitude) at 300 K under an inert atmosphere for the sample with the highest Te concentration (x=15%, δ=21%), for different times of measurements, after storage in low-vacuum conditions: 1 month after synthesis (Aug. 2022), 4 months after synthesis (Nov. 2022) and 10 months after synthesis (May 2023).

Supplementary Note 6: Transport properties

Another indication of ferroelectric properties in our single crystals can be found in the current vs voltage (IV) curves. Supplementary Figure 10 shows I-V measurements taken in samples from x=0% to 15%, at 300 K and 50 K. Undoped $WSe_{2(1-\delta)}$ samples show an S-shape symmetrical curve, characteristic of a semiconductor, both at 300 K and 50 K, with no signs of anomalies. In contrast, all other tellurium-doped samples show IV curves that are highly asymmetrical with respect to the voltage polarity (diode-like behavior), and with clear hysteretic behavior (resistive switching-like behavior, and/or capacitive hysteresis-like behavior). This type of behavior seems to be enhanced at low temperature for all Te-doped samples. It is worth highlighting that the hysteretic and asymmetric behavior present at 300 K for all Te-doped samples are commonly observed in prototypical ferroelectric materials such as $BaFeO_3$ and $BaTiO_3$, and the origin of this multifunctional (i.e., diode-like, resistive switching and capacitive hysteresis effects) is an active area of research, with multifunctional applications in electronic devices.

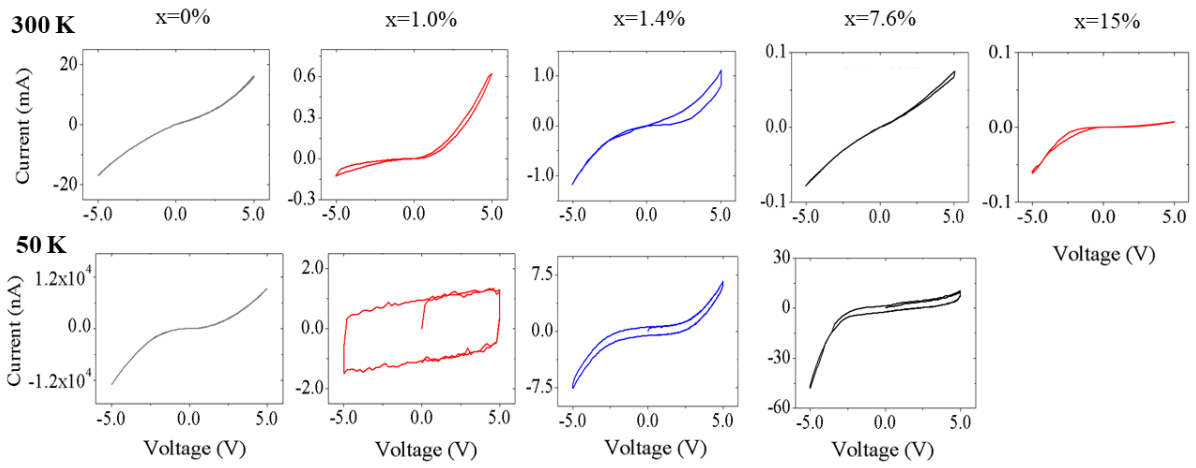

Supplementary Figure 10. Current-voltage curves. IV characteristics of undoped and Te-doped single crystals at 300 K (upper row) and 50 K (lower row).

Supplementary Note 7: DFT computed magnetization

The results of the DFT calculations for magnetic properties of $W(Se_{1-x}Te_x)_{2(1-\delta)}$ with different levels of Te doping and chalcogen vacancies, and for different atomic configurations, are presented in Supplementary Table 4 and Supplementary Figure 11.

x	δ	a(Å)	c(Å)	*Minimum number of W-Se(Te) bonds*	M (μ_B / *unit cell*) no SOC	M (μ_B / *unit cell*) SOC
0.0000	0.0000	3.289	12.999	6	0.0000000	0.0000000
0.0000	0.0000	3.29[73]	13.09[73]	6	-	-
0.0000	0.031250	3.267	12.946	5	0.000000000	0.000000156
0.0000	0.109375	3.209	13.135	5	0.000000000	-0.000000625
0.0000	0.390625	2.964	12.009	0	0.189400000	0.190000000
0.015625	0.0000	3.293	13.044	6	0.000000000	0.000000000
0.0625	0.0000	3.303	13.118	6	0.000000000	0.000000000
0.017544	0.109375	3.212	13.184	5	0.000000000	0.000000000
0.125	0.2187	3.134	13.103	5	0.000000369	-
0.102564	0.390625	2.961	13.092	0	0.177000000	0.177000000
0.102564	0.390625	2.923	14.043	2	0.000000000	-

Supplementary Table 4. Computed total unit cell magnetization, for different levels of Te-doping and chalcogen vacancies, with and without SOC. Last row corresponds to the structure of Supplementary Figure 11. For proper comparison, the lattice parameter a is the optimized supercell value (for x or $\delta \neq 0$) divided by 4. From the table it is clear that although SOC interactions affect the magnetization, they are small and could in principle be ignored. The largest magnetization is obtained for the highest vacancy level, independently of the Te-doping.

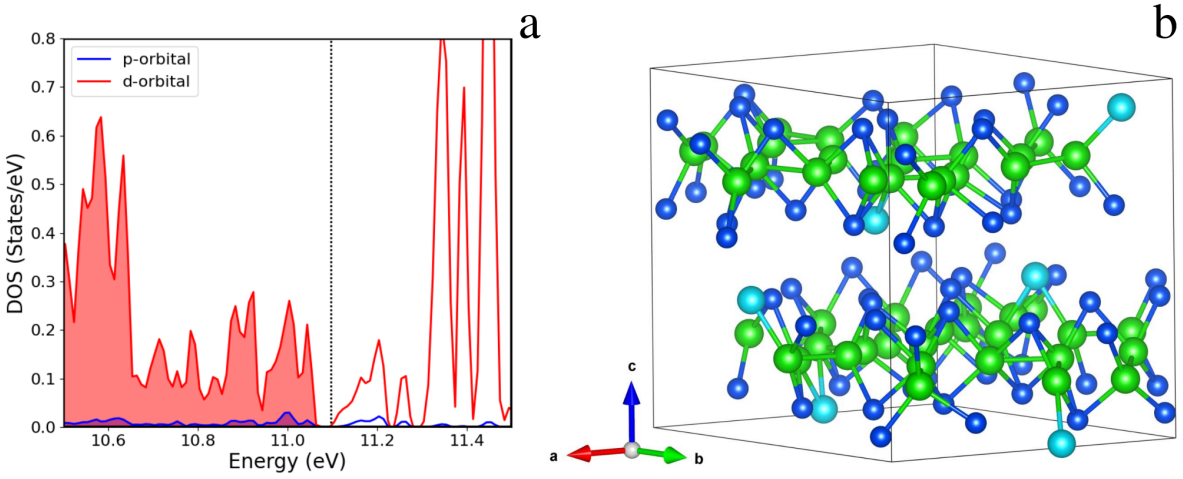

Supplementary Figure 11. DFT calculation for a non-magnetic realization. (a) Projected density of states on atomic orbitals of W1, the atom with the largest magnetic moment. **(b)** Optimized unit cell for a second configuration of $W(Se_{1-x}Te_x)_{2(1-\delta)}$ with x=10.26% and δ=39.06%. In this case all W atoms are bonded to at least one chalcogen atom and the resulting magnetization is zero.

Supplementary Note 8: DFT computed electric polarization

The results of the DFT calculations for the electric polarization of $W(Se_{1-x}Te_x)_{2(1-\delta)}$ with different levels of Te doping and chalcogen vacancies, and for different atomic configurations, are presented in Supplementary Table 5 and Supplementary Figures 12 and 13.

x	δ	*Hirshfeld charge* (10^{-2} a.u.)	P_x ($\mu C/cm^2$)	P_y ($\mu C/cm^2$)	P_z ($\mu C/cm^2$)
0.0000	0.0000	Q_W=-1.57 Q_{Se}= 0.79	0.00	0.00	0.00
0.102564	0.0000		4.09E-08	-1.51E-07	-7.98E-07
0.0000	0.390625	Q_{W27}=-7.46 Q_{W28}=-3.26 Q_{W32}=-10.33 Q_{Se7}=5.54	9.80	0.05	-9.95
0.102564 Se5 below vacancy	0.390625	Q_{W27}=-5.30 Q_{W28}=-2.52 Q_{W32}=-9.37 Q_{Se5}=3.31	-5.43	-4.06	-0.36
0.102564 Se5 above vacancy	0.390625	Q_{W27}=-5.86 Q_{W28}=-2.80 Q_{W32}=-9.62 Q_{Se5}=4.49	7.16	-0.44	6.04
0.102564 Te2 below vacancy	0.390625	Q_{W27}=-4.82 Q_{W28}=-4.20 Q_{W32}=-10.18 Q_{Te2}=8.64	0.58	-8.65	-5.54
0.125	0.2187		-0.71	3.12	4.7

Supplementary Table 5. Computed values for Hirshfeld charge of different atoms in the unit cell, and total unit cell electric polarization, for different values of Te-doping and chalcogen vacancies.

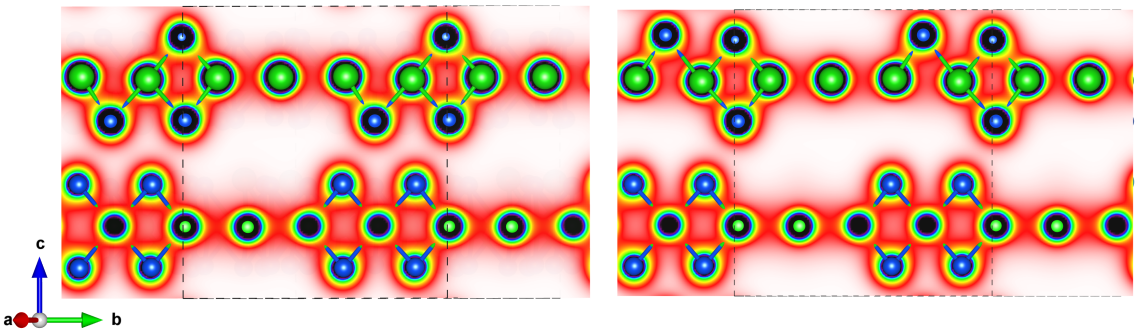

Supplementary Figure 12. DFT computed electronic densities. [1 0 0] views of the total electronic densities as obtained for the vacancy on top (left) and below (right) a Se atom.

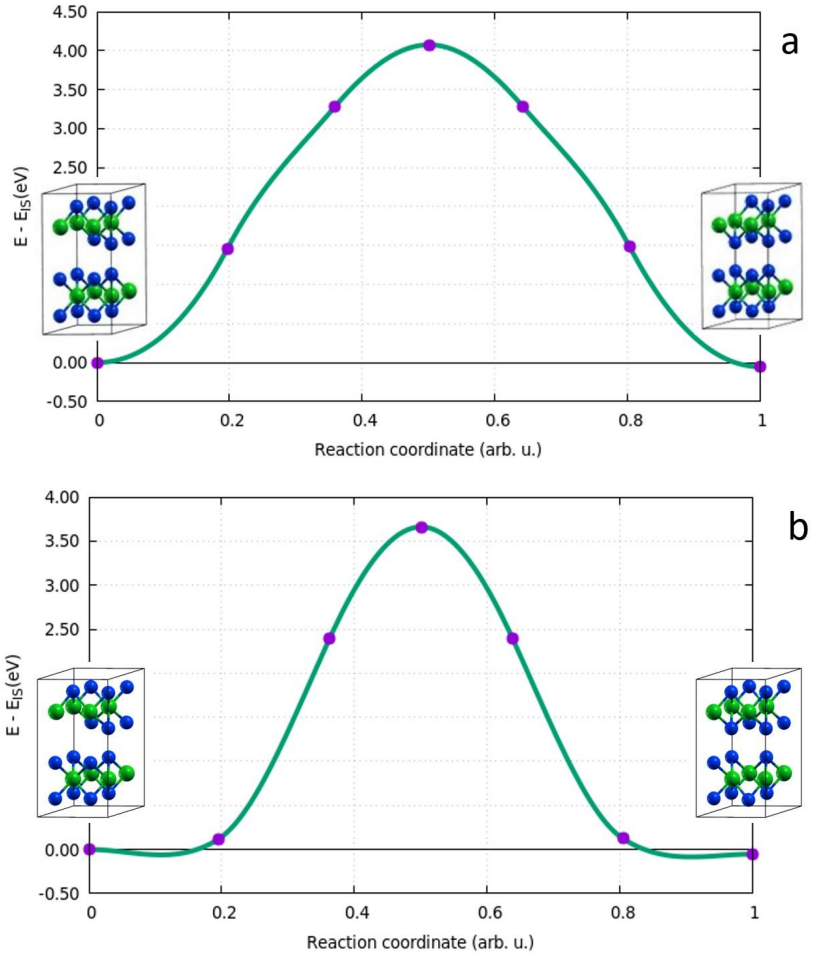

Supplementary Figure 13. NEB calculation of the energy barrier as a function of the reaction coordinate for **(a)** intralayer displacement of the vacancy and **(b)** interlayer vacancy diffusion in a 2 x 2 x 1 supercell system. Insets display initial and final images for each case, which were obtained by performing ionic relaxations. The final reaction paths and energy barriers are 4.41 Å, 4.1 eV and 4.97 Å, 3.67 eV for the intralayer and the interlayer vacancy displacement respectively.

Supplementary Note 9: List of included files in data repository.

The following files can be found publicly available in the repository: https://github.com/pgiraldogallo/RoomTmultiferroicityInTMDs-npj2DmatAppl.git, folder "SI_Files". Their description is as follows:

The crystallographic information filed - CIF - of the resolved crystal structure found by single crystal diffraction, for two of the studied compositions, can be found in the files:

Te-concentration	Files
x=1%	File S1: S1_WSeTe-1percent.cif File S2: S2_checkcif report for WSeTe-1percent.pdf
x=7.6%	File S3: S3_WSeTe-7percent.cif File S4: S4_checkcif report for Te-7percent.pdf

Computed atomic coordinates, lattice constants as well as Hirshfeld charge analysis for several configurations can be found in the following files:

Configuration	Files
x=6.25%, δ=39.0625% and Se5 atom below the vacancy.	File S5: S5_WSe2Te6.25Vac39-relaxed.xsf File S6: S6_Hirshfeld-Te6.525Vac39.txt
x=6.25, δ=39.0625% and Se5 atom above the vacancy.	File S7: S7_WSe2Te6.25Vac39-SeAbove.xsf File S8: S8_Hirshfeld-Te6.525Vac39-SeAbove.txt
x=6.25%, δ=39.0625% and Te2 atom below the vacancy.	File S9: S9_WSe2Te6.25Vac39-TeBelow.xsf File S10: S10_Hirshfeld-Te6.25Vac39-TeBelow.txt
x=6.25%, δ=39.0625% non-magnetic configuration.	File S11: S11_WSeTeVac-conf2-relaxed.xsf
x=0%, δ=39.0625% and Se5 atom below the vacancy.	File S12: S12_WSe2Te0.0Vac39.xsf File S13: S13_Hirshfeld-Te0.0Vac39.txt
x=16%, δ=21.87%	File S14: S14_WSeTe12.5Vac21.87-relaxed.xsf File S15: S15_Hirshfeld-WSeTe12.5Vac21.87.txt

Animated XSF files of the intralayer and interlayer ferroelectric switching as obtained from the NEB calculations, can be found in the following files:

File S16: S16_ Intralayer.axsf,
File S17: S17_Interlayer.axsf.